Icarus 333 (2019) 37–51

Contents lists available at ScienceDirect

Icarus

journal homepage: www.elsevier.com/locate/icarus

Geological characterization of the Chang'e-4 landing area on the lunar farside

Le Qiao*, Zongcheng Ling*, Xiaohui Fu, Bo Li

Shandong Provincial Key Laboratory of Optical Astronomy and Solar-Terrestrial Environment, Institute of Space Sciences, Shandong University, Weihai 264209, China

ARTICLE INFO

Keywords:
Chang'e-4/CE-4
Landing site
Farside volcanism
South Pole-Aitken basin/SPA basin
Lunar/Moon

ABSTRACT

On January 3, 2019, China's Chang'e-4 probe, accomplishes the first-ever soft landing on Moon's farside in the Von Kármán crater floor mare volcanism plain (177.59°E, 45.46°S) within the South Pole-Aitken (SPA) basin. Its surface *in-situ* measurements would provide the first "ground truth" for lunar farside volcanism and SPA materials. We present a detailed geologic context, topographical, morphological, quantitative geochemical and mineralogical characterization of a 20 × 20 km area centered at the Chang'e-4 landing site, using the latest multi-source high-resolution orbital data sets. The landing area is very flat at a baseline of 30 m, with 90% of surface having slope < 5°, and deficient of surface boulder exposures. The landing area mare is superposed by abundant sub-kilometer, block-poor circular impact craters and secondary craters in chains and clusters. Mare basalts at the landing site is dominated by low-titanium basalts, and appear to be less mafic and iron-depleted than all typical kinds of retuned lunar basalt samples and may represent a new kind of mare basalt. The landing site mare is heavily sculptured by a set of linear parallel ridged and furrowed textures formed by ballistic ejecta from the Finsen crater, which are characterized by a more feldspathic composition, while with elevated orthopyroxene abundance, and may represent compositional properties of the primitive SPA basin floor materials. We propose the Finsen ejecta and mare basalt outcrops at the landing area as prioritized targets for Chang'e-4 surface geological and spectroscopic explorations. Follow-on mission data interpretations should consider the mixing effect of local mare basalts and distant feldspathic materials.

1. Introduction: China's Change'e-4 mission to the lunar farside

Lunar farside, the hemisphere of the Moon that permanently faces away for the view of Earth due to tidal locking effect, has never seen by human before the Space Age and serves as a yearning destination for aeronautical exploration endeavors. In 1959, the Soviet Luna 3 mission first spotted the lunar farside and presented its fundamental difference from the nearside of the Moon. Since then, extensive remote sensing explorations over the past half century had revealed substantial knowledge of the lunar farisde, including Lunar Orbiter, Apollo (orbital observations), Clementine, Lunar Prospector, Kaguya, Chang'e-1/2, Chandrayaan-1, Lunar Reconnaissance Orbiter (LRO) and GRAIL. Numbers of lunar farside landed missions have ever been proposed, for instance, the farside Tsiolkovsky crater as the target for Apollo 17 crewed mission (Wilhelms, 1993), the MoonRise NASA mission concept (Jolliff et al., 2010) and the Farside Explorer proposed for ESA's Cosmic Vision program (Mimoun et al., 2012). However, due to many operational difficulties for lunar farside landing, especially communication relay and the highly rugged lunar farside surface, the lunar farside remains as an unexplored sector for soft-landing missions until today.

On January 3, 2019, China's Chang'e-4 (CE-4) probe, carrying the Yutu-2 rover, accomplished the first-ever soft landing on Moon's farside. The landing site (177.59°E, 45.46°S, Di, 2019) is located in the mare plain emplaced within the Von Kármán crater floor in the South Pole-Aitken (SPA) basin. The Chang'e-4/Yutu-2 will investigate the geological and compositional characteristics, and shallow subsurface structure of the landing area using its set of instruments including several cameras (namely Landing Camera, Terrain Camera and Panoramic Camera), Lunar Penetrating Radar (LPR) and Visible and Near-Infrared Imaging Spectrometer (VNIS) (Wu et al., 2017; Jia et al., 2018), with a much higher spatial resolution which cannot be achieved by previous and current remote sensing missions. Surface *in-situ* measurements implemented by the Chang'e-4 mission will provide the first "ground truth" for lunar farside and the SPA basin.

Recently, Huang et al. (2018) presented a remarkable documentation on the detailed 3-D geological characteristics of the Chang'e-4 landing target region (45.0–46.0°S, 176.4–178.8°E, ~50 × 30 km in size) using available remote sensing data, including surface

* Corresponding authors.
E-mail addresses: leqiao.geo@gmail.com (L. Qiao), zcling@sdu.edu.cn (Z. Ling).

https://doi.org/10.1016/j.icarus.2019.05.029
Received 21 January 2019; Received in revised form 16 May 2019; Accepted 20 May 2019
Available online 23 May 2019
0019-1035/ © 2019 Elsevier Inc. All rights reserved.

morphology, topography, mineral composition, regolith and ejecta thicknesses, stratigraphy and chronology, which provide an instructive framework for Chang'e-4 surface measurements. In this contribution, we build on the important initial survey by Huang et al. (2018) and present a dedicated geological characterization of the more local Chang'e-4 landing area (a 20 × 20 km area centered at the landing site) in a more insightful perspective using additional new multi-source high-resolution orbital data sets. We investigate (1) the regional geological context, (2) detailed and comprehensive topography, morphology and morphometry and (3) quantitative geochemistry and mineralogy of the 20 × 20 km landing area. These analysis results provide additional timely and noteworthy references for Chang'e-4 surface exploration planning and follow-on mission data interpretations.

2. Data and methodology

We first analyze the morphology and topography of the CE-4 landing area, including its geologic setting within the SPA basin, the Von Kármán crater and its vicinity, using the latest, moderate resolution images from the LRO Wide-Angle Camera (LROC WAC, 100 m/pixel, Robinson et al., 2010) and Kaguya/SELENE-TC (Terrain Camera) + LRO-LOLA (Lunar Orbiter Laser Altimeter) merged topography (SLDEM2015; 512 pixels/degree spatial sampling and ~3–4 m vertical altimetric accuracy; Barker et al., 2016). We then undertake a detailed characterization of the topography and morphology of the landing area using original LRO LOLA laser altimetric data (~10 cm altimetric precision; Smith et al., 2010), high-resolution Kaguya TC stereogrammetry digital terrain model (DTM) (10 m pixel size and ~3–4 m altimetric accuracy; Haruyama, 2012; Barker et al., 2014), Kaguya TC (10 m pixel size; Haruyama et al., 2008) and LROC Narrow-Angle Camera (LROC NAC, up to 0.60 m/pixel, Robinson et al., 2010) images. Each individual LROC NAC frame is generated from raw NAC EDR (experiment data record) image through photometrically correction and map-projection using the USGS's Integrated Software for Imagers and Spectrometers (ISIS3; *e.g.*, Anderson et al., 2004) according to the terms of the LROC EDR Data Products Software Interface Specification (Bowman-Cisneros, 2010). We investigate the iron and titanium elemental contents of the studied landing area based on Kaguya Multiband Imager (MI) data (20 m/pixel) using algorithms reported by Lemelin et al. (2015) and Otake et al. (2012), respectively. The errors for deriving the FeO and TiO_2 contents were estimated to be ~1 wt% and 0.43 wt%, respectively. At last, quantitative mineralogical analysis for major rock-forming minerals (olivine, orthopyroxene, clinopyroxene and plagioclase) is based on the global mineral abundance maps (60 m/pixel) produced by Lemelin et al. (2019) from Kaguya MI spectrometer data through radiative transfer modeling calculations. The Kaguya MI-extracted mineral abundance has an $1\sigma = 7$ wt% uncertainty from the Lunar Soil Characterization Consortium (LSCC) data (Taylor et al., 2001; Lemelin et al., 2019).

3. Results and interpretations

3.1. Geologic context of Chang'e-4 landing area

The Chang'e-4/Yutu-2 lander and rover combination successfully landed on the floor of the 186-km-diameter Von Kármán crater. The Von Kármán crater sits in the northwest central region of the SPA basin and is centered at 44.45°S, 176.25°E (LOLA 2011 control network). Its degraded topographic and morphologic characteristics had leaded earlier geologic mapping effort to designate it as a Nectarian-aged crater (Stuart-Alexander, 1978). Recent geologic mapping investigation reported an older, pre-Nectarian, ~3.97 Ga age for this crater (Yingst et al., 2016). The landing site is ~350 km northwest from the SPA ellipse center (53°S, 169°W) and ~700 km from SPA basin outer ellipse (Fig. 1A; Garrick-Bethell and Zuber, 2009). As the largest (2400 × 2050 km, Garrick-Bethell and Zuber, 2009), deepest (> 8 km; Petro and Pieters, 2004) and the oldest impact structure (more than four billion years old; *e.g.*, Hiesinger et al., 2012; Garrick-Bethell and Miljković, 2018) recognized on the Moon, the SPA basin should have excavated the deepest materials of lunar interior (maximum excavation depth up to over 100 km; *e.g.*, Schultz and Crawford, 2011; Potter et al., 2012). Recent numerical simulations show the SPA basin-formation impact should have certainly exposed lunar mantle materials to the farside surface (Melosh et al., 2017), yet spectroscopic studies revealed very spare occurrence of olivine (Lucey, 2004; Yamamoto et al., 2010, 2012; Ohtake et al., 2014). Having landed within the central region of this unique terrain of Moon, the expected surface *in-situ* geological and geochemical investigations of Chang'e-4 mission will provide an unprecedented opportunity to address a number of important questions regarding lunar basin formation and subsequent effects, earlier bombardment history of the Earth-Moon system (and even for the inner solar system), composition and physical characteristics of lunar deep interior (lower crust and possible lunar upper mantle) (NRC, 2007, 2011).

Regionally, the Von Kármán crater is located at the transition from the more rugged SPA basin rim structure to relatively flat (at the scale of hundreds of kilometers) basin floor (Fig. 1A). The Von Kármán crater is enclosed by several other large impact craters, namely Leibnitz in the north, Finsen in the northeast, Von Kármán M in the south and Oresme in the west (Fig. 1B). These impact craters are characterized by observable cross-cutting and superposition relationships, enabling us to establish the stratigraphic sequences of these craters. The Von Kármán M crater is clearly superposed and largely deconstructed (especially the northern rim; thus relatively older) by the Von Kármán crater. From the residual southern portion of the rim structure, the Von Kármán M crater has been estimated to have a diameter of ~245 km (Fig. 1B; Head III et al., 2010). The ~240-km-diamater Leibnitz crater lies in the immediate north exterior of Von Kármán crater. Emplacement of the south rim of Leibnitz crater has buried and deconstructed the north rim crest of Von Kármán crater. The Leibnitz impact event should have also spewed massive ejecta onto the northern floor of Von Kármán crater, resulting in its elevated topography and rugged and hummocky terrains (Fig. 1B). Recent geological study reported a Nectarian, ~3.88 Ga age for the Leibnitz crater (Yingst et al., 2016). The Oresme crater, with a diameter of ~76 km, seems to have comparable topographic degradation state with Von Kármán crater. Previous geologic mapping has attributed an ancient, pre-Nectarian age for this crater (Stuart-Alexander, 1978). The superposition relationship between the two craters cannot be unambiguously determined, while examination of new LROC WAC images show the development of the Oresme crater structure appears to has propagated into the exterior ejecta deposits of Von Kármán crater, suggesting Oresme probably postdate the Von Kármán crater (Fig. 1B). Another regional prominent feature is the 73-km-diameter Finsen crater to the northeast of Von Kármán crater. The Finsen crater is characterized by well-preserved primitive large crater structures, including wall terrains, continuous ejecta blanket and central peak formation. Extensive bright ray patterns and radial secondary craters are clearly observed, in optical images, to be associated with Finsen crater, which serve as diagnostic evidences to attribute Finsen crater as a Copernian-aged crater (Hawke et al., 2004). The mare deposits within Von Kármán and Leibnitz crater floors have been heavily superimposed by ejecta from the Finsen crater (Fig. 1B).

The Von Kármán crater itself is 186 km in diameter, with a rim-to-floor depth of ~3.5 km (Fig. 2), which shows the Von Kármán crater has a much smaller depth-to-diameter value than young (post-Imbrian) complex lunar craters (Kalynn et al., 2013); we attributed this to the ancient age, degraded topographic characteristics and subsequent lava filling within crater floor. New LRO altimetry and image data show this crater probably developed a ringed peak-cluster structure (though, poorly reserved, pointed out by arrows in Fig. 2B). From the potential remnants of this ringed peak-cluster structure, we measure a ~40 km ring diameter, which lies approximately on the trend line of ring

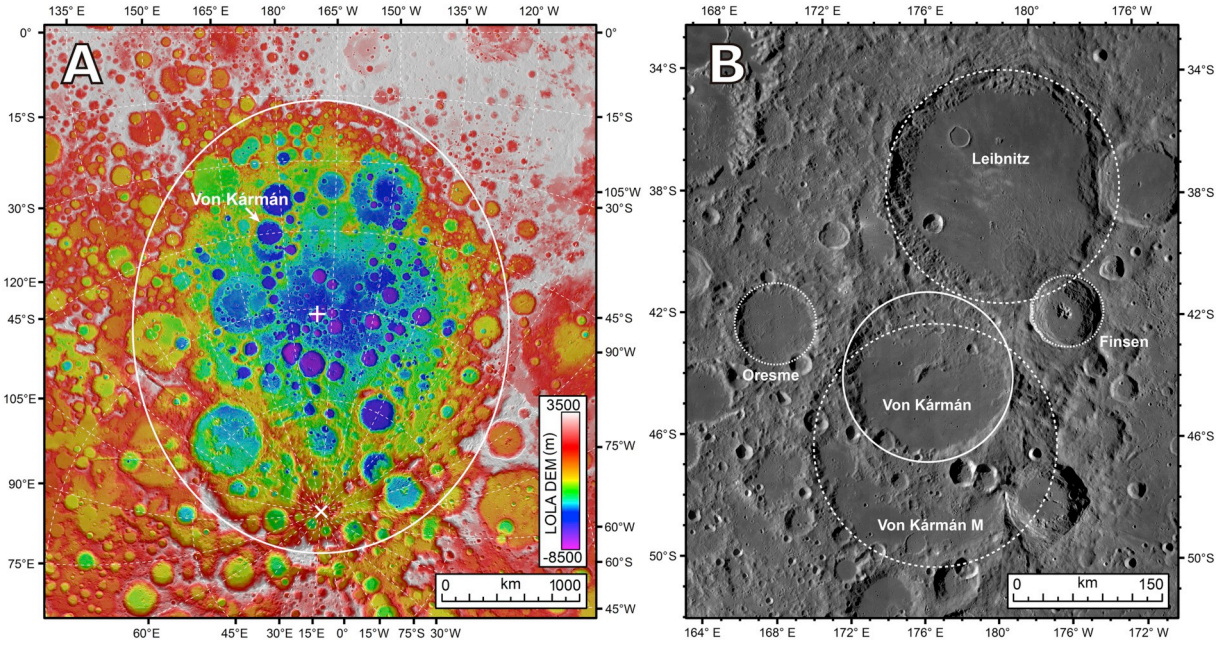


Fig. 1. (A) The topographic context of Von Kármán crater within the South Pole-Aitken (SPA) basin, LOLA DEM topography (128 pixel/degree) overlaid on LROC WAC mosaic. The white oval and cross mark the best-fit topographic outer ellipse and center of SPA basin, perspectivity (Garrick-Bethell and Zuber, 2009), the white multiplication sign marks the south pole, and the location of Von Kármán crater is pointed out. The projection is stereographic centered at 191°E, 53°W, and north is up. (B) The regional vicinity of Von Kármán crater, LROC WAC image mosaic. The bold white circle marks the rim locations of Von Kármán crater and the dotted white circles mark the rim locations of Von Kármán M, Leibnitz, Oresme and Finsen craters (Head III et al., 2010). The projection is lambert conformal projection, centered at 176°E, 44.5°S, and north is up.

diameter/rim-crest diameters for over 40 peak-ring and ringed peak-cluster basins on the Moon (Baker et al., 2011). Peak-ring craters/basins are generally regarded as a morphologic transition from smaller complex craters to multi-ringed basins, while the specific formation mechanism is still unknown and includes interpretations of downward and radial movement of the "displaced zone" below the transient cavity (Melosh, 1989; Spudis, 1993), differential scaling between crater sizes and volume of impact melt (*e.g.*, Grieve and Cintala, 1992), "nested melt-cavity" model (Head, 2010), emplacement of the outwardly collapsed crust basement above the collapsed transient cavity rim (Morgan et al., 2016), *etc*. The poor preservation state of the peak ring structure is probably a combined result from subsequent ejecta deposition (dominantly from Leibnitz crater), lava flooding and topographic degradation.

Topographic and compositional analyses can provide fundamental information of the geological characteristics and evolution history of the landing area. The Von Kármán crater interior floor is characterized by a wide range of topographic and morphological characteristics, and shows a distinct dichotomy between the northern and the southern portions (Fig. 2). The northern crater interior is dominated by ejecta deposits, with very rough and rugged surface textures (with slopes typically > 5°; Fig. 2D) and a typical highland, feldspar-dominated composition. The southern portion of crater interior is largely filled with mare lava deposits, characterized by relatively flat surface (with slopes dominantly < 4°; Fig. 2D) and an iron-rich basaltic composition. These mare plains occupy an area of 1.063×10^4 km^2. Elevation of the western mare is generally higher than the southern part, which show a topographic decline of ~350 m across a distance of ~80 km (Fig. 2B, C). Population study of superposed impact craters using Kaguya images reported a 3.35 Ga model age for the Von Kármán mare flows (Haruyama et al., 2009). An updated crater population study using LROC WAC images yielded a relatively younger model age of 3.15 Ga (Pasckert et al., 2018). In addition, Pasckert et al. (2018) also observed a second older model age of 3.75 Ga, which might be related to an older buried flow. Two bulge/dome-like structures are identified in the western margin of the interior mare units (pointed out by white triangles in Fig. 2B). The northern bulge is circular in shape, 14 × 16 km in diameter, and stands ~160 m from the surrounding flat mare unit (Fig. 3C, D). The southern bulge is irregular in shape, and shows coalescing outline patterns (Pasckert et al., 2018), with a measured size of 40 × 20 km; it stands nearly ~350 m from the surrounding mare (Fig. 3A, B). No summit endogenetic pits have been observed to be associated with these bulges. In addition, these bulges are characterized by comparable elevations with the relatively higher portion of the western mare units (Fig. 2B). These morphologic and topographic observations suggest, these bulges, along with the western mare regions, may represent the latest phase of volcanic lava infilling activities within Von Kármán crater floor.

The floor terrains within Von Kármán crater are superposed by abundant impact craters with a wide range of diameters, and the northern ejecta deposits and the southern mare deposits show significant impact population discrepancy (Fig. 2A). Five craters > 5 km in diameter are counted on the northern ejecta deposits, while all superposed craters on the southern mare is smaller than 5 km; this suggest a lengthy period between the deposition of the two surfaces, probably on the scale of billions of years. On the mare deposits, several relatively large (diameters up to ~4.8 km), fresh impact craters are identified, which are characterized by prominent ray patterns, ejecta blanket, and sharp rim structures (Fig. 2A).

3.2. General topography of the landing area

General topography analysis of the landing area can provide important information for the Chang'e-4 mission planning and scientific investigations. We first employ the original LOLA laser range (and inferred elevation) measurement spots (also known as "shots") of lunar surface to characterize the general topography of the landing area, as LOLA shots provide the highest altimetric precision (~10 cm; Smith et al., 2010). During years of operations, LOLA has accumulated over 70,000 measurements for the landing area (Fig. 4A). The total

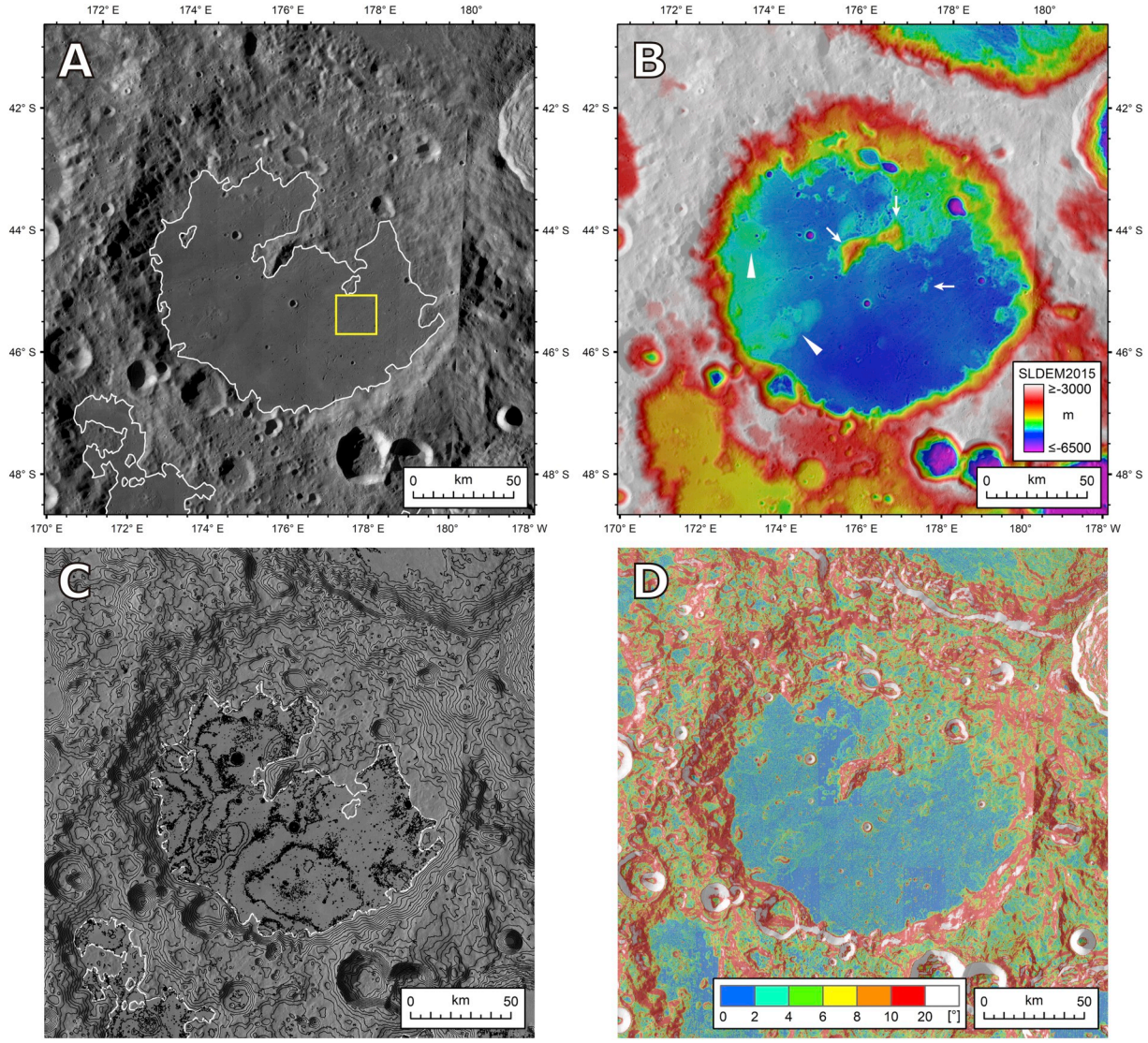


Fig. 2. Von Kármán crater: (A) LROC WAC image, the yellow square marks the studied 20 × 20 km landing area (Section 3) and the white outlines delineate the extent of mare basalt deposits, (B) SLDEM2015 (Kaguya/SELENE-TC + LRO-LOLA merged DEM) topography overlaid on WAC image, the white triangles points to the two bulge/dome-like structures (Fig. 3) and the white arrows mark the possible ringed peak-cluster structure, (C) contour map overlaid on WAC image, contour interval is 50 m for the mare region (outlined by white polygons) and 300 m for non-mare region, (D) SLDEM2015-derived slope map (baseline ~180 m) overlaid on WAC image. All panels are projected into lambert conformal projection, centered at 176°E, 44.5°S, and north is up. (For interpretation of the references to colour in this figure legend, the reader is referred to the web version of this article.)

topographic relief of the 20 × 20 km landing area is ~120 m (from about −6000 m to about −5880 m relative to the mean planetary radius), while the elevation of the vast majority of the surface (99.3%) ranges from −5960 m to −5900 m (Fig. 4B). Two elliptic areas, one in the west edge with a size of about 9 × 6 km and another one in the southwest corner with a size of about 7 × 3.5 km, are characterized by relatively lower elevations. These two elliptic areas are generally ~10–20 m lower than the rest portion of the studied landing area.

Despite the remarkable altimetric precision of LOLA shots, their sampling of topography of the landing area (a middle-latitude region) is still sparse (Fig. 4A). We alternatively refer to the Kaguya TC stereogrammetry DTM (Fig. 5), which provide excellent surface topography sampling (10 m/pixel) and spatial coverage (the entire landing area and ~99% of global lunar surface), though less accurate altimetric precision (~3–4 m; Haruyama et al., 2012; Barker et al., 2014). The elevation mapping results of the Kaguya DTM (Fig. 5A, B) is generally consist with the large-scale topography revealed by the LOLA shot measurements (Fig. 4A), while provide substantial topographic details of small geologic features. On the high-resolution Kaguya DTM maps, the most prominent features are abundant depressions with size ranging from 100 s of meters to over one kilometer. Most of these relatively small depressions are generally circular in map view, which should be normal lunar impact craters. The several relatively large depressions (> ~1 km) are, however, dominated by irregular elongate and furrowed patterns, indicating they are more likely grooves sculptured by ejecta debris from distance basins/craters (Section 3.3; Huang et al., 2018). In addition, pervasive parallel ridges are observed in the south and east parts of the studied area, where Chang'e-4/Yutu-2 landed on. These ridges extend dominantly in the NE-SW direction, radial to the Finsen crater, indicating they may represent Finsen impact ejecta debris and deposits (Section 3.3; Huang et al., 2018).

Kaguya TC DTM-derived topographic slope map, with a baseline of 30 m, shows the entire landing area is very flat, with 90% of surface having slopes < 5° (Fig. 5C,D), which would definitely facilitate surface exploration efforts, including rover navigability and mobility, and surface operations and experiments. Local elevated slopes (> 5°)

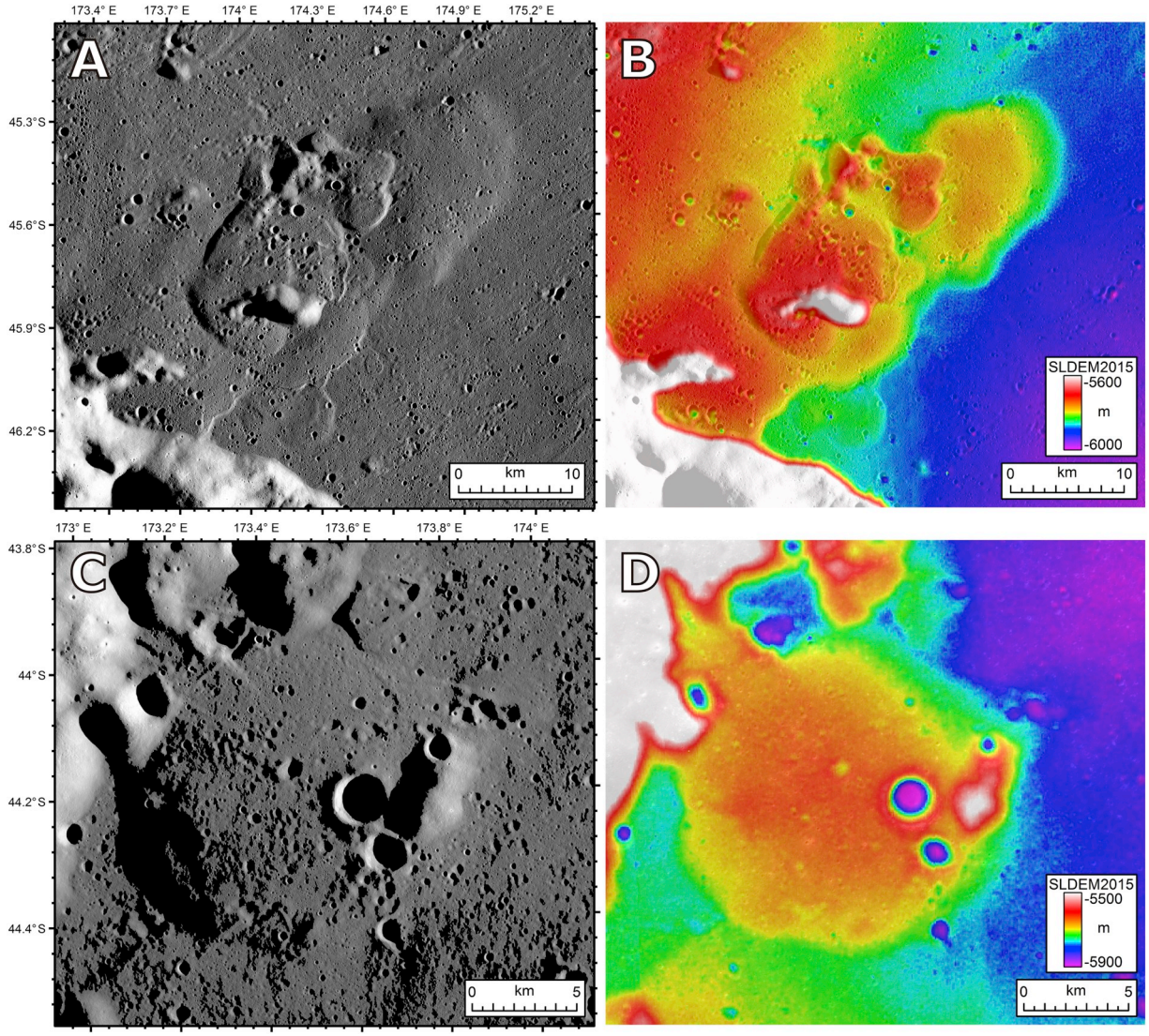


Fig. 3. The two dome-like structures (upper panels: the north one; lower panels: the south one) observed at the western margin of Von Kármán crater floor mare (Fig. 2B): (A, C) Kaguya TC image mosaic map and (B, D) SLDEM 2015 topography overlain on TC mosaic. All panels are projected into lambert conformal projection, centered at 176°E, 44.5°S, and north is up.

mainly occurs at the inner walls of relatively larger (> ~200 m in diameter) and well-preserved impact craters. NE-SW-trending ridges, while as prominent features on the topography maps (Fig. 5A, B), are indistinguishable on the slope maps, which may be ascribed to the less altimetric precision and longer baseline of the slope data.

3.3. Morphology of the landing area

Morphology analysis can identify various resultant deposits of many geological processes, thus providing us an insight into the regional geological evolution history of the landing area. In the studied landing area, the major landforms are very flat mare lava plain deposits (Figs. 5C and 6), typical for lava-filling impact basins/craters on the lunar nearside. Similar with mare plain elsewhere on the Moon, lava flow fronts and eruption vents/fractures are not observed within the landing area, suggesting the regional lava-filling are characterized by relatively low effusion rate, cooling-limited lava flows (Head and Wilson, 2017; Qiao et al., 2016a, 2016b), and/or the initially emplaced lava flow morphology has been largely degraded. In addition, other endmember volcanic features, like volcanic cones, pyroclastic deposits, mare domes, sinuous rilles, are not identified in the studied area, showing the regional volcanic eruptions are relatively less complicated than other volcanic concentrations on the Moon. Examination of submeter LROC NAC images (up to ~0.60 m/pixel) show the landing area surface is highly deficient of surface boulder exposures, verified by surface images returned from the Chang'e-4/Yutu-2 (*e.g.*, panoramic image obtained by Terrain Camera onboard the lander: http://www.cnsa.gov.cn/n6759533/c6805143/content.html). This contrasts with the Chang'e-3/Yutu landing area, where the regional mare surface is dotted with many small rock fragments and abundant boulders occurring within and surrounding several craters (Basilevsky et al., 2013; Qiao et al., 2016b, 2016c). The observed surface blockiness discrepancy can be attributed to the much older surface model age of the Chang'e-4 landing area mare (over 3 Ga; the Chang'e-3 mare can be as young as ~2 Ga (Morota et al., 2011)) and (the resultant) thicker surface regolith layer.

Circular craters (likely mainly primary impact craters) are the dominant morphologic features superposed on the landing area mare surface (Fig. 6). The largest circular impact crater occurs at the southeastern edge of the studied landing area (Fig. 6) and has a diameter of ~1.1 km and a rim-to-floor depth of ~150 m. These superposed craters are characterized by a wide range of preservation status,

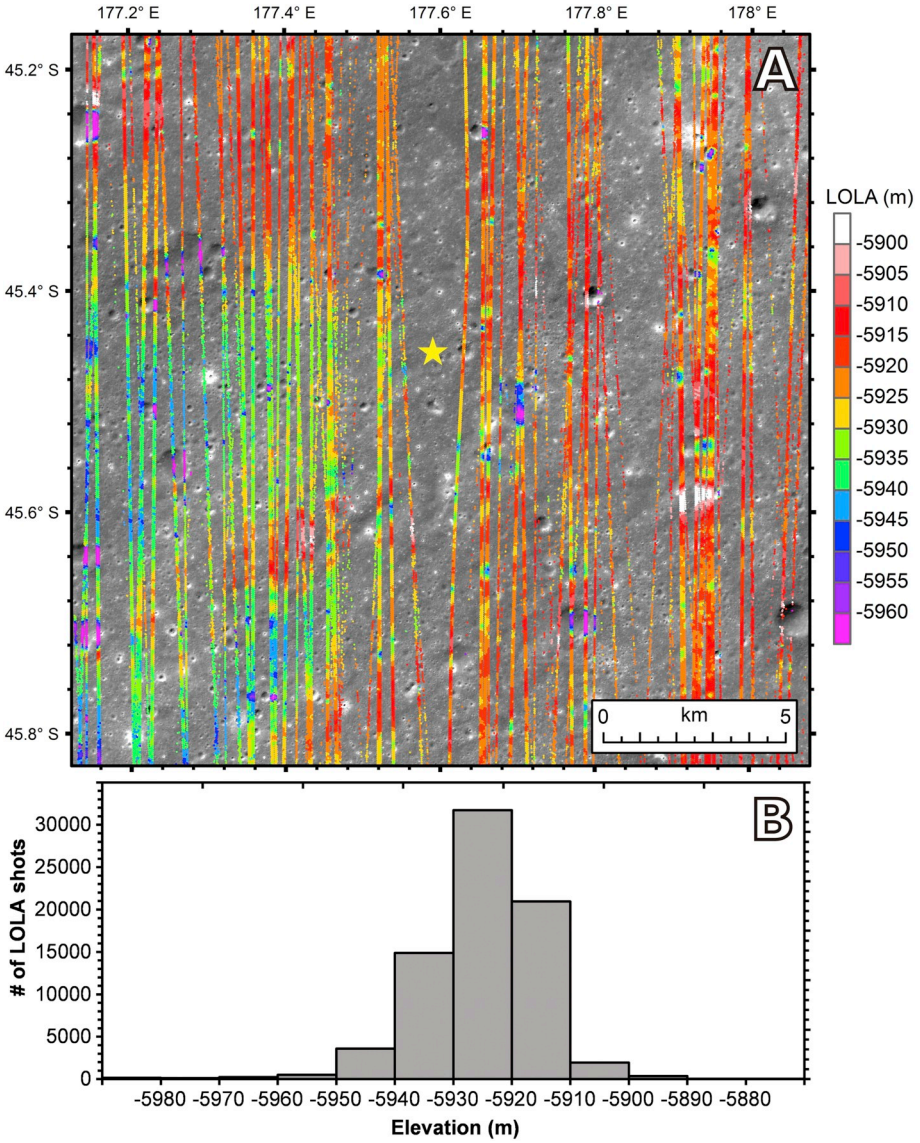


Fig. 4. (A) LOLA RDR (Reduced Data Record) shot elevation measurements of Chang'e-4 landing area, overlain on Kaguya TC image mosaic, and (B) their histogram. The yellow star in panel A denotes the Chang'e-4 landing site. All the maps for the studied landing area in this paper are projected into a lambert conformal projection, centered at 177.6°E, 44.5°S, and north is up. (For interpretation of the references to colour in this figure legend, the reader is referred to the web version of this article.)

ranging from fresh carters with sharp rim structures (Fig. 7A) and highly degraded craters nearly beyond recognition (Fig. 7B). At the moderately-sloped (~5°) walls of these degraded crater, elephant hide-like textures are frequently observed (arrow pointed out in Fig. 7B); these are generally interpreted as indicator of regolith creep motion (*e.g.*, Melosh, 2011). Circular impact craters are generally deficient of boulders in crater interior and ejecta blanket (Fig. 7B). A few very fresh craters have developed extensive bright ray pattern, ejecta and scattered boulders (Fig. 7A), which represent the least mature materials in the studied landing area. However, these fresh craters are still much less blocky than blocky craters in other landing sites, like the Cone crater (Apollo 14) and Zi Wei crater (Chang'e-3).

Another group of prominent landforms in the landing area is the suite of features related to secondary impact cratering, including elongate, chains or clusters of small craters radial to the source primary crater (Fig. 7C, D), and individual irregular craters with "herringbone" shapes (Fig. 6). These secondaries also show a wide range of preservation states; however, they generally lack ray patterns and blocky ejecta (even for those with the best preservation status), indicating these secondary craters were formed by much less energetic events than primary impact cratering. Their distinctive morphological patterns provide instructive insights for tracking their source region. Recent work by Huang et al. (2018) present remarkable morphological characterization and origin analyses of these secondary craters. In particular, they traced the relatively large, north-south trending secondaries (pointed out in Fig. 6) to the Antoniadi crater in the over 700 km south. However, detailed mapping of Antoniadi secondaries showed Antoniadi was formed by an oblique impact with the projectile coming from the northwest, and the Von Kármán crater lies in distant up-range direction, where secondary craters should be much less abundant (Sruthi and

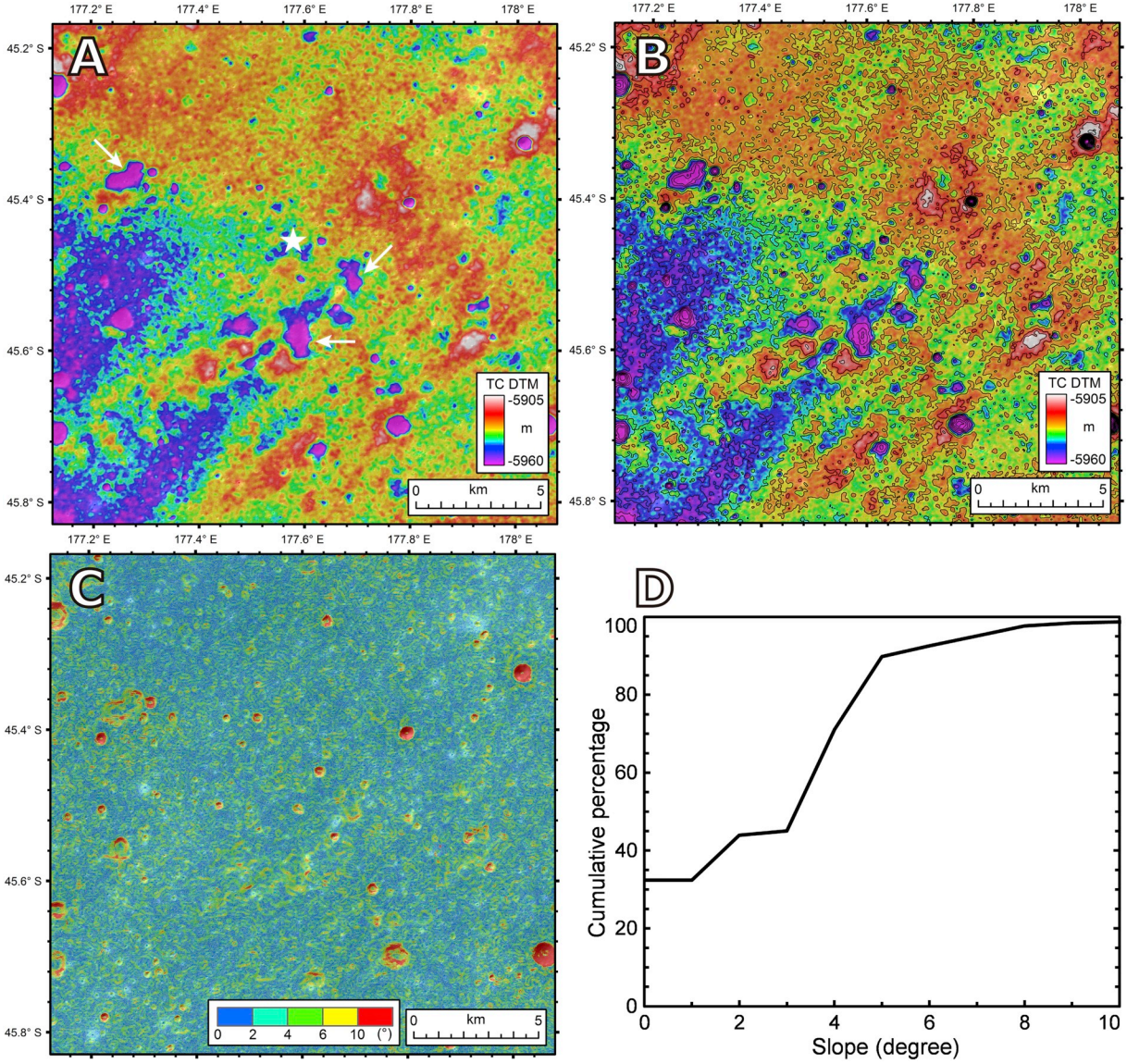


Fig. 5. Kaguya TC topography maps of the Chang'e-4 landing area: (A) TC DTM topography (10 m/pixel) overlain on TC image mosaic, (B) 10 m-interval contours overlain on topography, (C) TC DTM-derived slope map overlain on TC image mosaic and (D) the cumulative percentage distribution of slopes with 1° interval. In panel A, the white star denotes the Chang'e-4 landing site and the white arrows point to the relatively large, elongate depressions.

Kumar, 2014). We suggest other relatively large and young craters along the north-south trend can be additional source crater candidates, including Boyle (57 km), Abbe (64 km), Abbe H (25 km) and Minnaert (137 km) (Fig. A1 in Appendix B).

A prominent set of linear parallel ridged (Huang et al., 2018) and furrowed textures is observed on high-resolution Kaguya (Fig. 6) and LRO images. This lineament set consists of two major components: broad parallel ridges ~0.3 to 1.2 km wide and up to ~20–40 km in length (extending beyond the studied landing area) and a series of smaller parallel grooves hundreds of meters wide and up to ~5 km long. This distinctive texture is prevalently arranged in the NE-SW direction and radial to the Finsen crater, indicating they are genetically related with the Finsen impact. Similar radial textures, though much larger, has been observed and documented around a number of lunar impact basins including Imbrium and Orientale (Hartmann, 1963, 1964; Head, 1976; Schultz and Crawford, 2016). Given the relatively smaller size of the Finsen crater (compared with giant impact basins), these radial textures are more likely to be sedimentary in origin due to the erosional and depositional effects by ballistic ejecta from the Finsen crater-forming impact (Head, 1976). Kaguya TC DTM topography (Fig. 5A) measurements shows the heights of these ridges can be up to ~6 m, consistent with estimated Finsen crater ejecta thickness at the studied landing area (Huang et al., 2018). These lineament features, especially the deposited ridges, should contain a considerable portion of distant foreign materials from the Finsen crater, and Chang'e-4/Yutu-2 just landed on this Finsen ejecta-bearing area. This may provide additional scientific chances for Chang'e-4/Yutu-2 surface *in-situ* geological and compositional measurements, given the landing area mare lava plain is relatively homogeneous in surface characteristics and materials of the SPA-basin floor materials have been buried; the latter host the compositional information and other important characteristics of SPA impact basin, which is one of the key scientific questions of lunar and

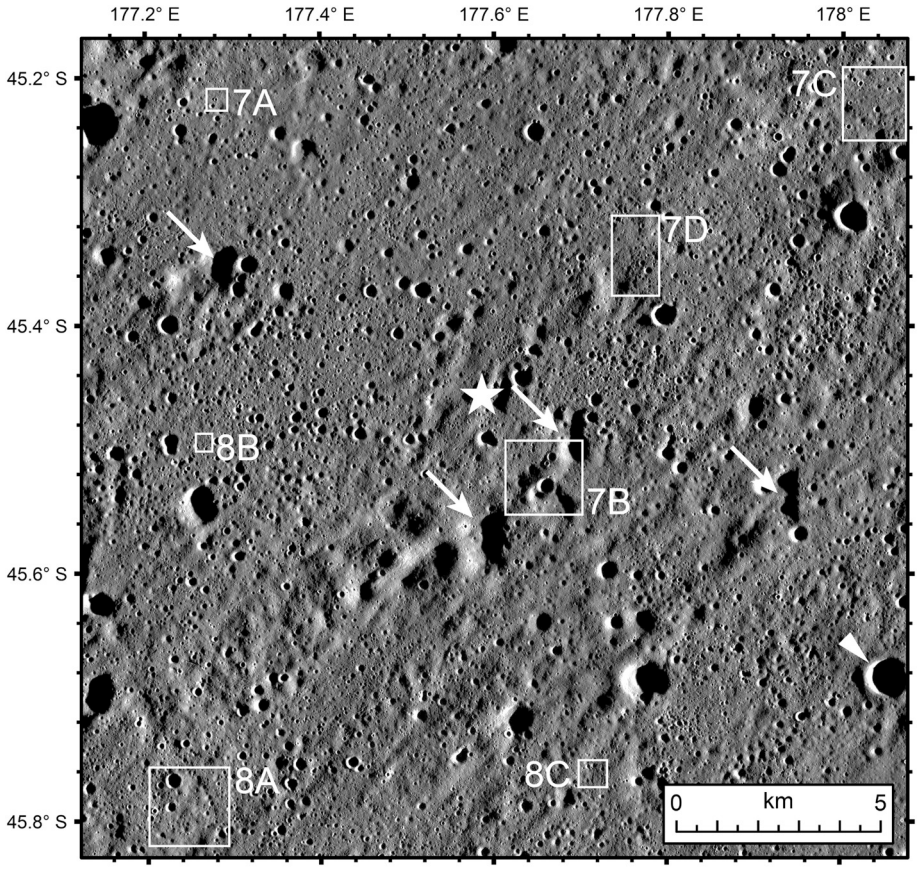


Fig. 6. Kaguya TC mosaic map (10 m/pixel) of the studied 20 × 20 km landing area. The white star denotes the Chang'e-4 landing site, the white triangle points to the largest circular impact crater in the landing area, white arrows point to the relatively large, north-south trending secondary craters and the white boxes show the locations of Figs. 7 and 8.

planetary science (NRC, 2007, 2011). Parallel linear grooves in NW-SE trend, while much smaller (10–40 m wide and 100–600 m long) are also observed at the southwest corner of the studied landing area (Fig. 8A), indicating a genetic relation to craters other than Finsen, like the 82-km-diameter Alder crater in the southeast vicinity.

We also find a number of small sinuous troughs, generally 20–40 m wide and 200–350 m long, in the lava plain of the studied landing area (Fig. 8B, C). Abundant similar sinuous ridges have also been documented in the vicinity of a fresh ~3.8-km-diamter crater ~20 km west of the studied landing area (Huang et al., 2018). While the spatial occurrence density of these sinuous troughs is much less sparse in the landing area, indicating a potential genetic relation to impact events, like impact-induced seismic disturbance of local surface and shallow subsurface substrates, which awaits on-going geophysical investigations by the Yutu-2 ground penetrating radars.

3.4. Chemical composition of the landing area

Kaguya MI-derived elemental maps show the studied landing area is fairy homogeneous in surface iron and titanium contents, especially for titanium content (Fig. 9). The majority (> 80%) of the landing area has calculated FeO content between 11 and 13 wt% and > 95% of the regional surface has TiO_2 content between 1 and 2 wt%. This estimated titanium content is comparable with Apollo 15 pigeonite basalts (Papike et al., 1976) and reveals the landing area mare deposits are dominated by low-titanium basalts (Giguere et al., 2000).

High-resolution iron mapping by Kaguya MI spectrometer image also reveals considerable geochemical variations across the studied landing area (Fig. 9A, B). Firstly, the studied landing area surface can be divided into two major units with slightly different iron contents: a northern belt region with relatively elevated FeO abundance (~13–14 wt%, mean value of 13.3 wt% with 1δ = 0.7) and a broader region with slightly lower FeO abundance (~12–13 wt%, mean value of 12.7 wt% with 1δ = 0.7). A null hypothesis test is performed to show the mean FeO abundance of the Finsen ejecta unit is statistically different from that of the north mare unit (Appendix A and Table A1). Cross-check with iron mapping at a much large extent covering the entire Von Kármán crater and its surroundings (Ling et al., 2019) shows the south low-iron unit, on which Chang'e-4 landed, belongs to a much more extensive region radial to the Finsen crater, suggesting the low-iron signature may represent compositional characteristics of Finsen ejecta materials or a mixture of Finsen ejecta and local mare basalts. Geomorphological investigation on Kaguya TC images also show the south portion are superposed with many linear parallel ridged and furrowed textures radial to the Finsen crater (Section 3.3 and Fig. 6), further supporting the Finsen ejecta origin of these low-iron materials. The composition of the northern belt region is probably more close to that of landing area mare deposits, which shows the landing area basalts are more iron-depleted than most of the typical kinds of lunar basalt samples returned by Apollo and Luna missions (Papike et al., 1976; Fig. 11) and *in-situ* measured by Chang'e-3 mission (Ling et al., 2015; Zhang et al., 2015; Fig. 11). If the MI-measured composition (mostly of regolith) is representative of that of the local primitive basalts, the mare basalts at the Chang'e-4 landing area may represent a unique kind of lunar basalts with decreased iron content, even when the typical 2 wt% FeO offset difference between lunar soil and basalts is considered (Gillis et al., 2004). Alternatively, this observed low-iron signal may be subject to the contamination of distant feldspathic ejecta

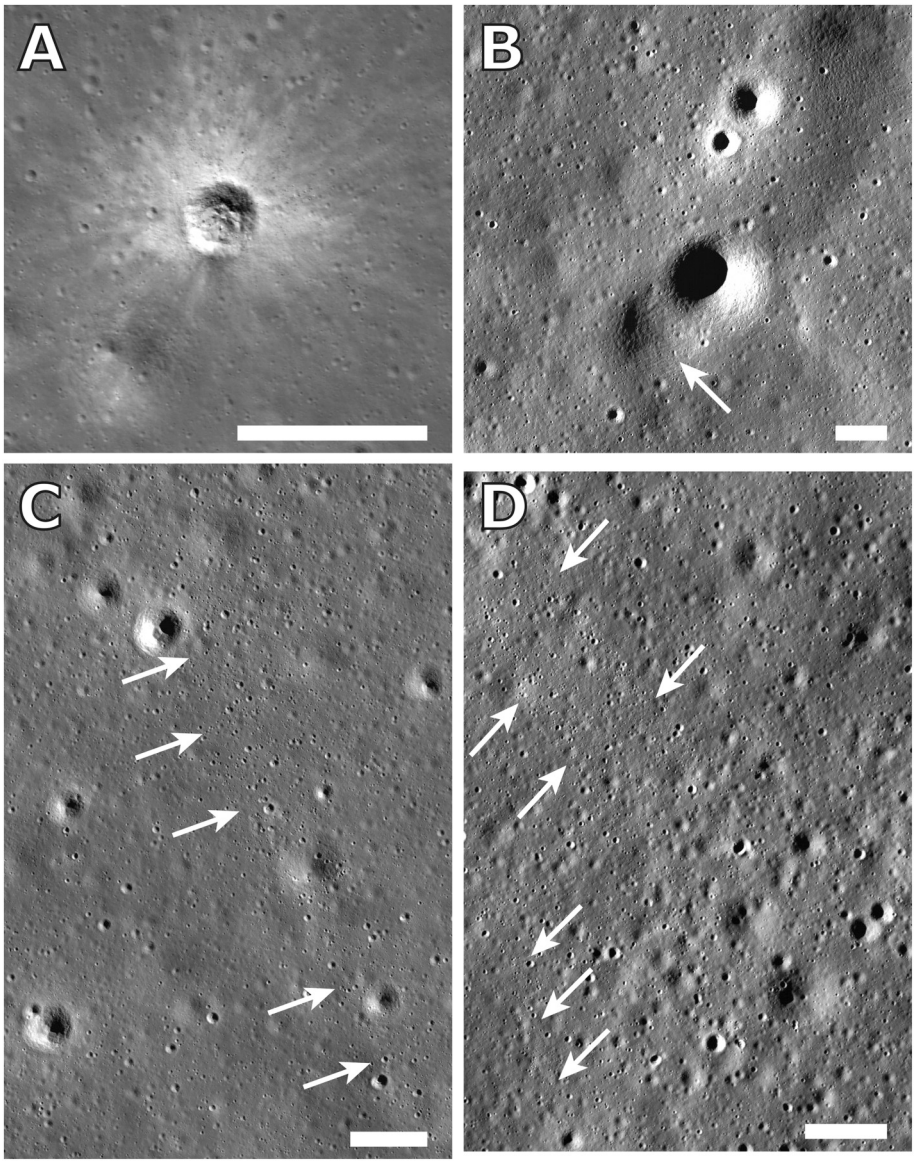


Fig. 7. (A) One of the regional freshest circular impact craters, ~80 m in diameter, at the northeast corner of the landing area, LROC NAC frame M189435642L, 0.62 m/pixel, 54.3° incidence angle. (B) Local surface ~1.5 km southeast from the landing site, shows several relatively large craters (~100–400 m diameter), with different preservation status, LROC NAC frames M134022629L/R, 1.27 m/pixel, 77.6° incidence angle. The arrow points to elephant hide-like textures at the walls of a degraded crater. (C, D) Second crater chains and clusters (marked by aligned arrow sets) in the northeast of the landing area, LROC NAC frame M161142858L (1.16 m pixel size and 71.6° incidence angle) for panel C, and M134022629R (1.27 m pixel size and 77.6° incidence angle) for panel D. The scales are all 200 m.

materials, which awaits clarification from the on-going Chang'e-4 surface *in-situ* investigations. Secondly, tens of regionally larger craters (~330 m–1.1 km diameter) are observed to have slightly iron-rich interiors and ejecta blankets (> 14 wt% FeO), suggesting a potential compositional inhomogeneous subsurface basaltic layer. These crater ejecta is also characterized by slightly elevated titanium content (~2–3 wt%) than the surrounding background mare plain (Fig. 9C). From the estimated depths of these craters (0.084 × crater diameter; Melosh, 1989), the depth of the underlying iron-rich basalts, also the thickness upper limit of the surface lava deposits, can be constrained to be ~30–90 m. Moreover, we also identified several strip-shape regions dotted by abundant small pits with decreased iron content (10–12 wt% FeO; Fig. 9A). We interpreted these low-iron characteristics in these strip-shape regions as ejectas from other distant craters, with lower iron content than Finsen crater ejecta.

3.5. Mineral composition of the landing area

Kaguya MI-retrieved mapping results of major rock-forming minerals (60 m/pixel; Lemelin et al., 2019) reveal that the studied landing area has average estimated mineral abundances of 7 wt% olivine (1δ = 3%), 24 wt% orthopyroxene (1δ = 4%), 14 wt% clinopyroxene (1δ = 4%), and 54 wt% plagioclase (1δ = 5%), with a total abundance of mafic component of 46 wt% (1δ = 5%) (Fig. 10). Kaguya MI spectral profiles of small fresh impact craters are characterized by absorptions at the 950 nm band (Fig. A2), indicating orthopyroxene as the dominant mafic component. The two major surface units, the north mare plain unit and the south Finsen ejecta unit identified based on topographic (Section 3.2), morphologic (Section 3.3) and geochemical (Section 3.4) investigations, are also easily distinguished on the mineral abundance maps. The mare unit materials are slightly more mafic than Finsen ejecta-bearing materials near the landing site, with relatively higher average olivine (9 ± 3 wt%) and clinopyroxene (16 ± 4 wt%) abundances (Fig. 10A, C, E). The mare basalts at the studied landing area seems to be much less mafic (total mafic mineral abundance of 48 ± 5 wt%) than returned lunar mare basaltic samples from several locations on lunar nearside (Lucey et al., 2006), suggesting mare basalts emplaced at the landing site on lunar farside may present a new kind of

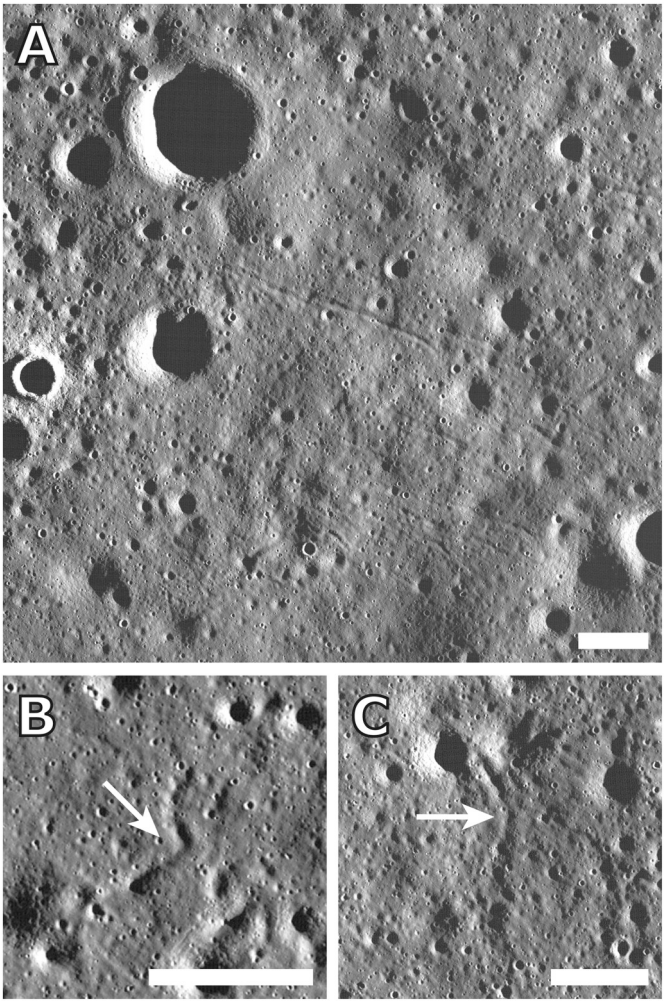


Fig. 8. (A) NW-SE trending linear grooves in the southwest corner of the landing area, LROC NAC frame M134022629R, 1.27 m/pixel, 77.6° incidence angle. Sinuous troughs at the (B) west margin (LROC NAC M161142858L) and (C) south margin (LROC NAC M134022629R) of the landing site. The scales are all 200 m.

mare basalts. Alternatively, this less mafic composition may be subject to contamination from the feldspathic eject debris from Finsen crater, surface *in-situ* spectroscopic measurements by Yutu-2 VNIS at the specimen-scale show great potentials for resolving this uncertainty. The Finsen ejecta unit contains more feldspathic components, with an estimated average plagioclase abundance of 45 ± 4 wt%, showing the Finsen impact has spewed considerable amount of feldspathic highland materials to the landing site on the Von Kármán crater floor mare deposits. In addition, the Finsen ejecta unit also has slightly higher orthopyroxene abundance (25 ± 4 wt%) than the mare unit (23 ± 4 wt %) (A null hypothesis test is performed to show the difference between the mean orthopyroxene abundance of the Finsen ejecta unit and the north mare unit is statistically significant (Appendix A and Table A1)), consistent with the recent M^3 spectroscopic identification of low-calcium pyroxene-bearing materials ejected from the Finsen crater (Huang et al., 2018).

Regional large craters also exhibit mineral compositional anomalies, indicating vertical mineralogy variations. Several large craters (~600 m to ~1.1 km in diameter) superposed on south Finsen ejecta unit are characterized by relatively elevated clinopyroxene abundance, but comparable with that of the north mare unit (pointed out in Fig. 10C), suggesting these craters have penetrated the overlying Finsen ejecta and exposed the underlying more mafic basaltic materials, consistent with the identification of high-calcium pyroxene-bearing components through M^3 spectroscopic analysis (Huang et al., 2018). In addition, the iron-rich craters (Section 3.4) also exhibit higher olivine and total mafic component abundance, suggesting the underlying (up to ~30–90 m deep) iron-rich basalts are also more olivine-rich.

4. Discussion and references for surface exploration planning and *in-situ* measurement interpretations

Our detailed geological characterization of the very local landing area presented above provide substantial context and references for Chang'e-4/Yutu-2 surface exploration mission planning and subsequent *in-situ* measurement interpretations. Mare basaltic deposits at the landing area appear to much less mafic than previously collected and *in-situ* measured lunar basalt samples (Papike et al., 1976; Lucey et al., 2006; Ling et al., 2015), with an estimated average FeO content of ~13 wt% and a total mafic mineral abundance of ~48 wt% (Sections 3.4, 3.5 and Fig. 11). In addition, a possible underlying basaltic layer at a depth up to ~30–90 m, characterized by slightly higher iron and titanium contents, olivine and total mafic mineral abundances, is identified, but it is still much less mafic than typical returned lunar basalts from lunar nearside. These unique less mafic signatures suggest the Chang'e-4 landing area basalts may represent a new type (or more new types) of mare basalts (and/or be contaminated by low-iron feldspathic ejecta materials) and surface *in-situ* spectroscopic investigations by Yutu-2 VNIS will provide an extraordinary opportunity to characterize lunar farside basalts and volcanism at a much finer scale which has been hardly achieved by previous and current orbital investigations.

The landing area mare plain is heavily superimposed by ejecta deposits dominantly from the Copernian-aged 73-km-diameter Finsen crater to the northeast and the Chang'e-4 just landed on this Finsen ejecta-bearing unit. The Finsen ejecta-bearing unit is characterized by a more feldspathic composition (higher plagioclase abundance and lower iron, olivine and clinopyroxene contents), but elevated orthopyroxene abundance. Being located at the central portion of the enormous SPA basin, Finsen impact-exposed materials would inevitably bring compositional and geological information of parts of the primitive SPA basin floor materials. This provides a remarkable occasion for Chang'e-4 surface geological and compositional measurements, given the SPA materials have been largely buried by subsequent mare lava flows at the landing area. Previous spectroscopic and geologic studies have presented substantial evidences that SPA materials contain more mafic components than the highland feldspathic crust, with the pervasive occurrences of low-Ca pyroxenes (*e.g.*, Tompkins and Pieters, 1999; Pieters et al., 2001; Cahill et al., 2009; Hurwitz and Kring, 2015; Moriarty III and Pieters, 2018). However, the specific origin of these SPA materials and their implications for a number of key questions regarding lunar deep interior composition, multi-ring basin formation mechanism and earlier lunar evolution and bombardment history are highly debated and includes scenarios of differentiated impact melt sheet (*e.g.*, Vaughan and Head, 2014; Hurwitz and Kring, 2015), exposures of lunar lower crust and/or upper mantle materials (*e.g.*, Pieters et al., 2001; Ohtake et al., 2014) or Mg-suite intrusions (*e.g.*, Klima et al., 2011). Yutu-2 surface *in-situ* spectroscopic measurements will provide the first “ground truth” for assessing these hypotheses.

As a landed mission, Chang'e-4 will provide a unique view of lunar farside volcanism and SPA-formation than orbital remote sensing missions. Though orbital spectroscopic measurements of lunar surface have been greatly improved in spatial sampling resolution over the past decades, the current highest resolution measurements (down to ~20 m

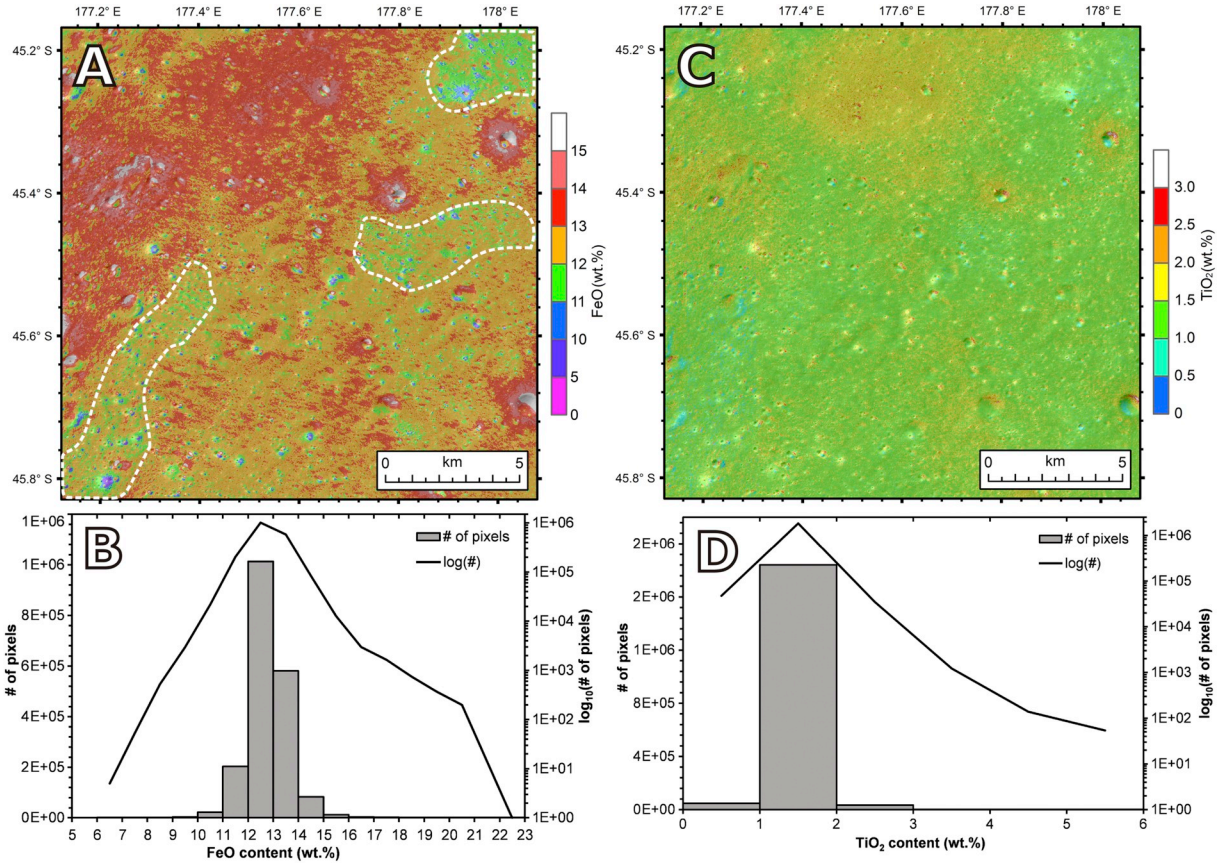


Fig. 9. FeO (A) and TiO_2 (C) abundance maps of the studied landing area (overlain on Kaguya TC image mosaic) and their histograms (B and D), calculated from Kaguya MI mosaic using the Lemelin et al. (2015) and Otake et al. (2012) algorithms, respectively. The dashed patches in panel A marks the strip-shape areas with decreased iron contents.

pixel size provided by Kaguya MI) are still subject to spectral mixing effect. Our orbital data-based geological study also shows the Chang'e-4 landing area is characterized by complicated mixing of local mare basalts, distant ejected feldspathic materials and other possible ejecta materials. Combined analyses with surface images obtained by a set of cameras and VNIS spectroscopic measurements at the specimen-scale would permit us to pinpoint the detailed origin and characteristics of specific targets, especially surface boulder exposures.

In summary, we suggest Finsen ejecta materials occurring at the parallel linear ridged and furrowed patterns (should be easily recognized in Chang'e-4/Yutu-2 surface images, *e.g.*, Chang'e-4 lander panoramic image: http://www.cnsa.gov.cn/n6759533/c6805143/content.html), and mare basalts exposed in the vicinity of craters of variable diameters as prioritized targets for surface *in-situ* geological and spectroscopic measurements, as their geological context and origin can be better understood and contain important information regarding to lunar farside volcanism and SPA basin formation. Surface small boulders exposed at the landing region surface are also important measuring objects, as they are subject to the least degree of mixing effect and preserve the primitive compositional information. Interpretations of Chang'e-4/Yutu-2 regolith measurements should consider the mixing effect of local mare basalts and distant feldspathic materials.

5. Conclusions

On the basis of detailed geological characterization of the Chang'e-4 landing area presented above, we draw the following conclusions:

(1) The Chang'e-4/Yutu-2 landed on the floor of the pre-Nectarian-aged Von Kármán crater, in the northwest central portion of the SPA basin of lunar farside, the largest and oldest identified impact structure on the Moon. The Von Kármán crater is enclosed by several regionally large craters, some of which postdate the Von Kármán crater and have spewed ejecta materials to Von Kármán crater floor.

(2) Locally, the Chang'e-4 landing site is located on the mare basalt plain emplaced at the south floor of Von Kármán crater. The local landing area (20 × 20 km) is very flat at the baseline of 30 m, with 90% of surface having slope < 5°, and deficient of surface boulder exposures, which should facilitate Yutu-2 surface roving and experiments.

(3) The major morphologic features superposed on the landing area mare are sub-kilometer circular impact craters, which generally lack boulders in crater interior and surrounding ejecta. Secondary craters, occurring in chains or clusters, are also pervasive in the landing area.

(4) The mare basalts at the landing area is dominated by low-titanium

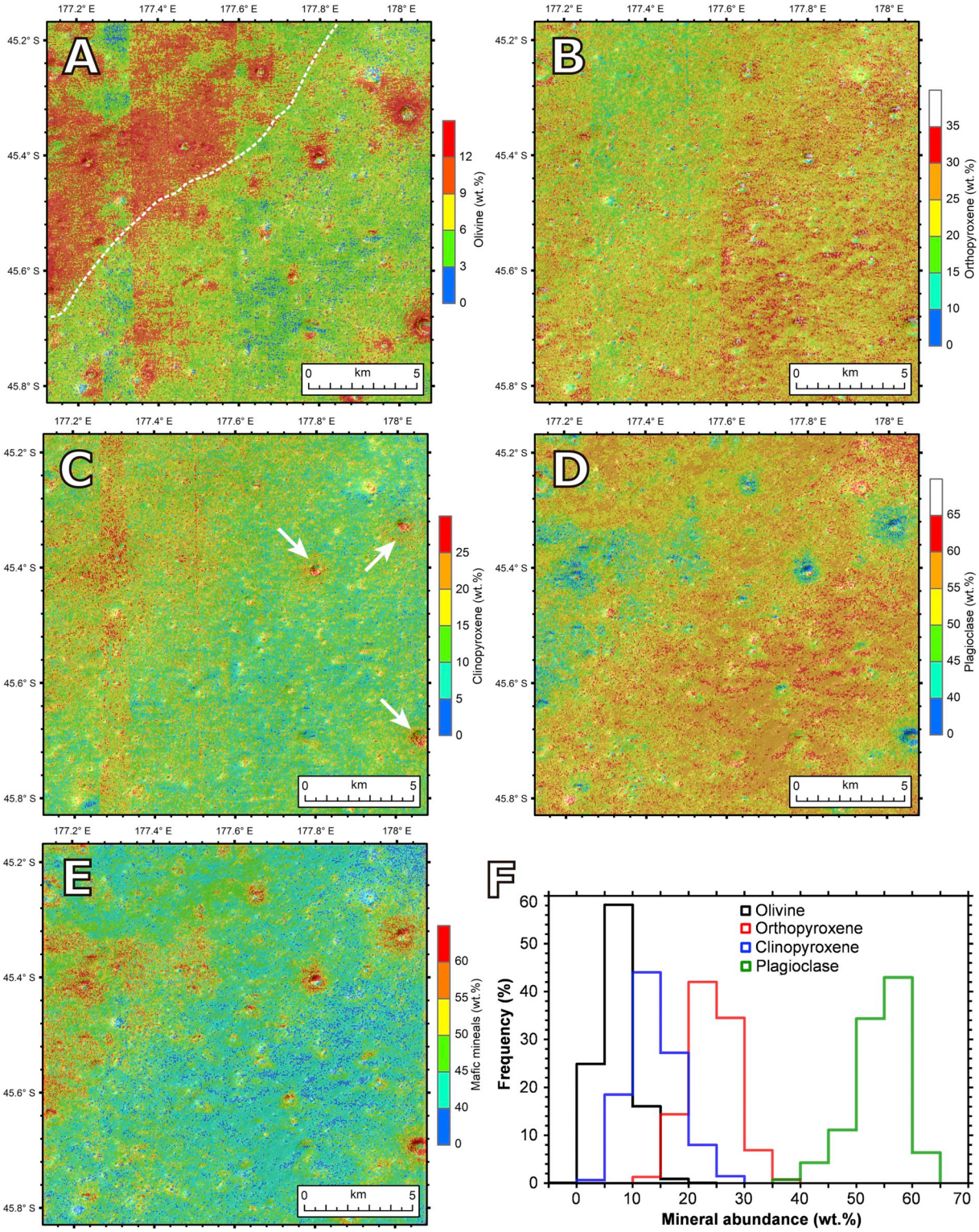


Fig. 10. Kaguya MI-retrieved abundance mapping results (Lemelin et al., 2019) of major rock-forming minerals of the studied landing area (overlain on Kaguya TC image mosaic): (A) olivine, (B) orthopyroxene, (C) clinopyroxene, (D) plagioclase, (E) mafic minerals, and (F) their histogram in percentage frequency in 5 wt% interval. The arrows in panel C point to the several craters with elevated clinopyroxene abundance. The dashed line in panel A delineates the boundary of the north mare plain unit and south Finsen ejecta unit (Section 3.4 and Fig. 9A).

basalts, and appear to be less mafic and more iron-depleted than most of the typical kinds of returned lunar basalt samples, suggesting the landing site mare basalt may represent a new type of mare basalts, or are subject to considerable level of contamination by distant low-iron materials. A possible underlying mare layer at a depth up to ~30–90 m, with slightly higher abundances of iron element and mafic minerals, is identified. Surface *in-situ* spectroscopic measurements by Yutu-2 VNIS will provide the first "ground truth" of lunar farside volcanism.

(5) The Chang'e-4 landing site mare is heavily sculptured by a set of

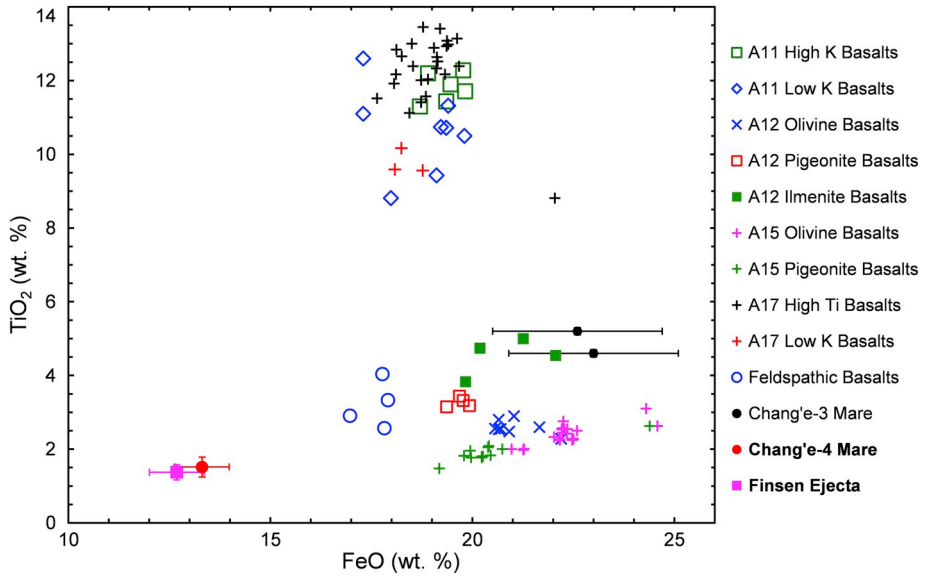


Fig. 11. Comparison of iron and titanium contents for mare basalts and Finsen crater ejecta materials at Chang'e-4 landing site (average values ± 1δ) with all typical kinds of lunar basalts (Papike et al., 1976) and Chang'e-3 surface *in-situ* measurements (Ling et al., 2015).

linear parallel ridged and furrowed textures formed by ballistic ejecta from the Copernian-aged Finsen crater. These Finsen ejecta materials have a more feldspathic composition, with elevated orthopyroxene abundance, and may represent compositional properties of the primitive SPA basin floor materials. Yutu-2 surface *in-situ* spectroscopic measurements of these materials would provide key information of SPA basin formation and lunar deep interior.

(6) We propose the Finsen ejecta and mare basalt outcrops present at the landing area as prioritized targets for Chang'e-4/Yutu-2 surface geological and spectroscopic explorations. Follow-on mission data interpretations should consider the mixing effect of local mare basalts and distant feldspathic materials.

Acknowledgments

We sincerely appreciate the Editor-in-Chief Rosaly Lopes for her very efficient and helpful editorial handling, and the reviewers for evaluating this work. This work is partly supported by the Open Fund of State Key Laboratory of Remote Sensing Science (Grant Nos. OFSLRSS201807 and OFSLRSS201802), National Natural Science Foundation of China (No. 41703063), China Postdoctoral Science Foundation (Nos. 2018T110682 and 2017M610421) and Natural Science Foundation of Shandong Province (JQ201511 and ZR2019MD015). All original LRO data can be found in the NASA's Planetary Data System (http://pds.nasa.gov/), the original Kaguya/SELENE data are archived at SELENE Data Archive (https://darts.isas.jaxa.jp/planet/pdap/selene/) and the Kaguya Multiband Imager mineral maps are available from the United States Geological Survey at the Planetary Data System's Cartography and Imaging Sciences Node Annex (http://astrogeology.usgs.gov/pds/annex).

Appendix A. Null hypothesis test

Independent samples *t*-test is performed to assess whether the MI-retrieved mean FeO content and orthopyroxene abundance of the Finsen ejecta units at the Chang'e-4 landing site are statistically different from those of the north mare unit (Sections 3.4, 3.5 and Figs. 9A, 10B in the main text). The null hypothesis is that the population means of the Finsen ejecta unit and the mare unit are equal. If the t value of our data is greater than t distribution critical value at a given confidence level (*i.e.*, 95%), then the null hypothesis is rejected. The null hypothesis test results are presented in Table A1, which shows the calculated t values are all greater than the t distribution (two-tailed) critical values at 95% confidence level. Thus, the null hypothesis can be rejected and the FeO content and orthopyroxene abundance differences between the Finsen ejecta unit and north mare unit are statistically significant.

Table A1
Results of null hypothesis tests for assessing whether the Kaguya MI-retrieved mean FeO content and orthopyroxene abundance differences between Finsen ejecta and the north mare unit are statistically significant. N is the number of MI FeO or orthopyroxene abundance map pixels in each analyzed unit, df is degree of freedom, t is t value of our data, and t_c is t distribution (two-tailed) critical value at the 95% confidence level.

Composition	Mare			Finsen ejecta			df	t	t_c
	N	Mean value	1σ	N	Mean value	1σ			
FeO (%)	553,918	13.3	0.7	898,368	12.7	0.7	1,452,284	541.79	1.96
Orthopyroxene (%)	49,284	23	4	80,205	25	4	129,487	120.47	1.96

Appendix B. Additional figure

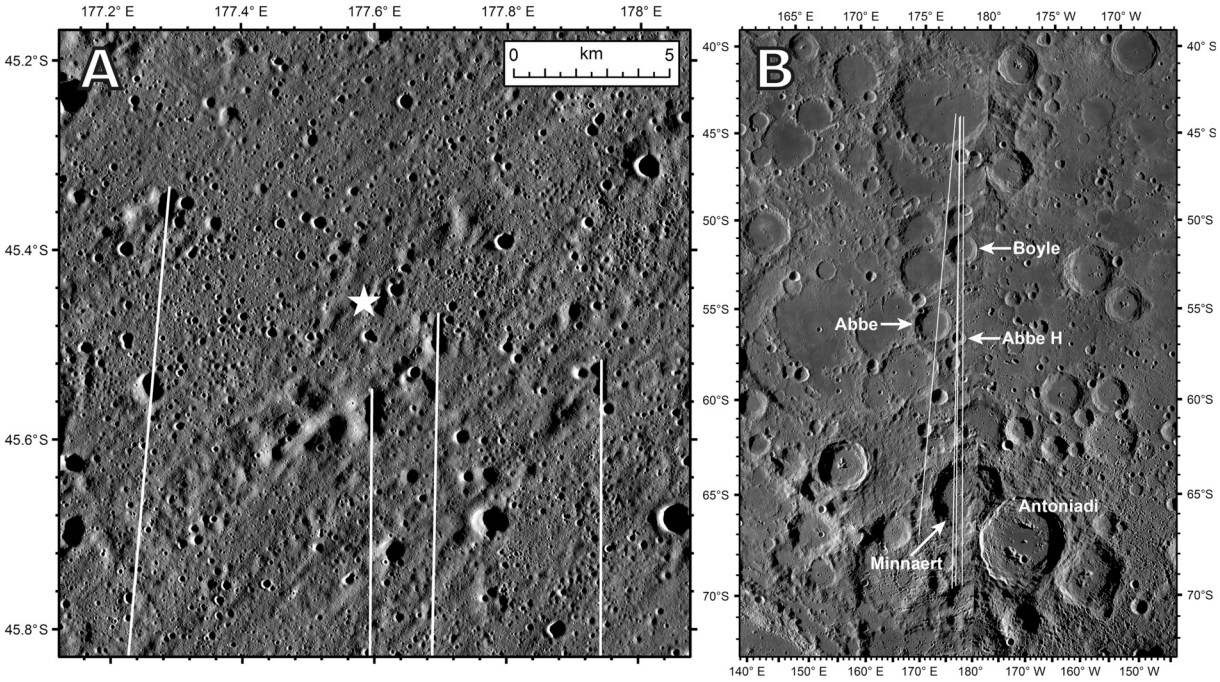


Fig. A1. (A) Local relatively large north-south trending secondary craters observed at the studied 20 × 20 km landing area, the white star denotes the Chang'e-4 landing site and the white lines mark trend of these secondaries, which locate at the starting point of the lines. Kaguya TC image mosaic, projected into a lambert conformal projection, centered at the landing site (177.6°E, 44.5°S), and north is up. (B) Great circles extended from trends of these secondaries. Several large craters along the trend are identified as additional source crater candidates other than Antoniadi, LROC WAC image mosaic in a same projection of panel A.

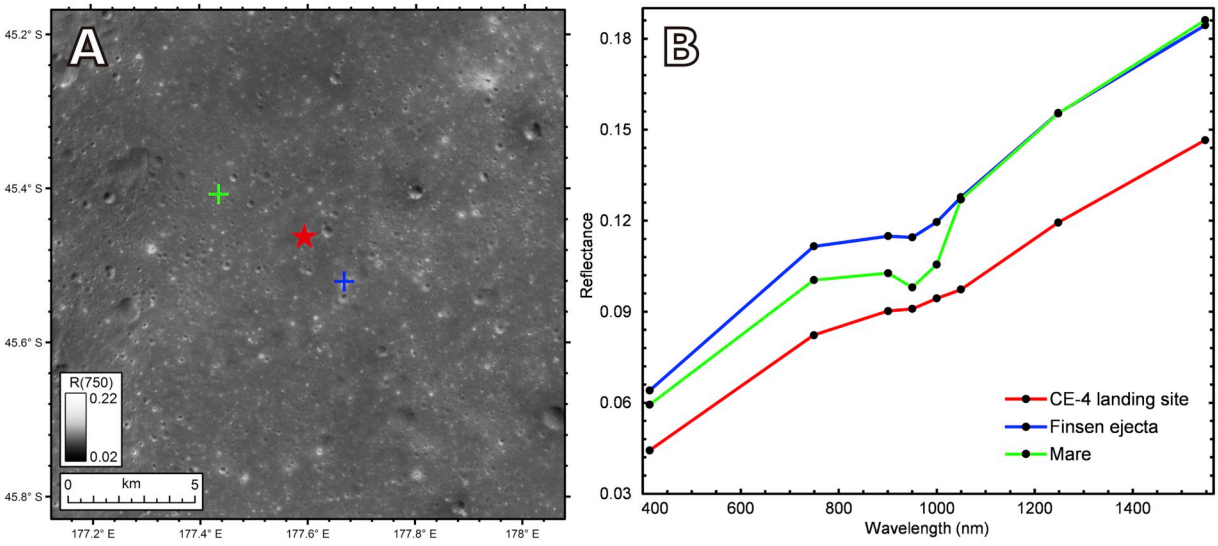


Fig. A2. (A) Kaguya MI 750 nm reflectance (R(750)) map and (B) MI spectral profiles of the Chang'e-4 landing site (its location marked by the red star in panel A) and two small fresh craters in the south Finsen ejecta unit (blue cross in panel A) and north mare plain unit (green cross in panel A). The systematic differences between the near-infrared (NIR) band data and ultraviolet-visible (UVVIS) data have been corrected (Lemelin et al., 2015) and the spectral profiles in panel B are given as averages of 4 × 4 pixel windows to increase the signal to noise ratios.

References

Anderson, J.A., Sides, S.C., Soltesz, D.L., Sucharski, T.L., Becker, K.J., 2004. Modernization of the Integrated Software for Imagers and Spectrometers. In: 35th Lunar and Planetary Science Conference. Lunar and Planetary Institute, League City, Texas (abstract #2039).

Baker, D.M.H., et al., 2011. The transition from complex crater to peak-ring basin on the Moon: new observations from the Lunar Orbiter Laser Altimeter (LOLA) instrument. Icarus 214, 377–393.

Barker, M.K., Mazarico, E., Neumann, G.A., Smith, D.E., Zuber, M.T., 2014. Merging digital elevation models from the Lunar Orbiter Laser Altimeter and Kaguya Terrain Camera. In: 45th Lunar and Planetary Science Conference. Lunar and Planetary Institute, The Woodlands, Texas (abstract #1635).

Barker, M.K., Mazarico, E., Neumann, G.A., Zuber, M.T., Haruyama, J., Smith, D.E., 2016. A new lunar digital elevation model from the Lunar Orbiter Laser Altimeter and SELENE Terrain Camera. Icarus 273, 346–355.

Basilevsky, A.T., Head, J.W., Horz, F., 2013. Survival times of meter-sized boulders on the surface of the Moon. Planet. Space Sci. 89, 118–126.

Bowman-Cisneros, E., 2010. LROC EDR/CDR Data Product Software Interface

Specification. Retrieved from. http://lroc.sese.asu.edu/data/LRO-L-LROC-2-EDR-V1.0/LROLRC_0001/DOCUMENT/LROCSIS.PDF.
Cahill, J.T.S., Lucey, P.G., Wieczorek, M.A., 2009. Compositional variations of the lunar crust: results from radiative transfer modeling of central peak spectra. J. Geophys. Res. Planets 114, E09001.
Di, K.C., et al., 2019. Chang'e-4 lander localization based on multi-source data. J. Remote. Sens. 23 (1), 177–184.
Garrick-Bethell, I., Miljković, K., 2018. Age of the lunar South Pole-Aitken basin. 49th Lunar and Planetary Science Conference. Lunar and Planetary Institute, The Woodlands, Texas (abstract #2633).
Garrick-Bethell, I., Zuber, M.T., 2009. Elliptical structure of the lunar South Pole-Aitken basin. Icarus 204, 399–408.
Giguere, T.A., Taylor, G.J., Hawke, B.R., Lucey, P.G., 2000. The titanium contents of lunar mare basalts. Meteorit. Planet. Sci. 35, 193–200.
Gillis, J.J., Jolliff, B.L., Korotev, R.L., 2004. Lunar surface geochemistry: global concentrations of Th, K, and FeO as derived from lunar prospector and Clementine data. Geochim. Cosmochim. Acta 68, 3791–3805.
Grieve, R.A.F., Cintala, M.J., 1992. An analysis of differential impact melt-crater scaling and implications for the terrestrial impact record. Meteoritics 27, 526–538.
Hartmann, W.K., 1963. Radial structures surrounding lunar basins, I: the imbrium system. Commun. Lunar Planet. Lab. 2, 1–16.
Hartmann, W.K., 1964. Radial structures surrounding lunar basins, II: Orientale and other systems; Conclusions. Communications of the Lunar and Planetary Laboratory, vol. 2. pp. 175–191.
Haruyama, J., et al., 2012. Lunar global digital terrain model dataset produced from SELENE (Kaguya) Terrain Camera stereo observations. In: 43rd Lunar and Planetary Science Conference. Lunar and Planetary Institute, The Woodlands, Texas (abstract #1200).
Haruyama, J., et al., 2008. Global lunar-surface mapping experiment using the Lunar Imager/Spectrometer on SELENE. Earth Planets Space 60, 243–255.
Haruyama, J., et al., 2009. Long-lived volcanism on the lunar farside revealed by SELENE Terrain Camera. Science 323, 905–908.
Hawke, B.R., et al., 2004. The origin of lunar crater rays. Icarus 170, 1–16.
Head, J.W., 1976. Evidence for the sedimentary origin of Imbrium sculpture and lunar basin radial texture. Moon Planets 15, 445–462.
Head, J.W., 2010. Transition from complex craters to multi-ringed basins on terrestrial planetary bodies: scale-dependent role of the expanding melt cavity and progressive interaction with the displaced zone. Geophys. Res. Lett. 37.
Head III, J.W., et al., 2010. Global distribution of large lunar craters: implications for resurfacing and impactor populations. Science 329, 1504–1507.
Head, J.W., Wilson, L., 2017. Generation, ascent and eruption of magma on the Moon: new insights into source depths, magma supply, intrusions and effusive/explosive eruptions (part 2: predicted emplacement processes and observations). Icarus 283, 176–223.
Hiesinger, H., et al., 2012. New crater size-frequency distribution measurements of the South Pole-Aitken basin. In: 43rd Lunar and Planetary Science Conference. Lunar and Planetary Institute, The Woodlands, Texas (abstract #2863).
Huang, J., et al., 2018. Geological characteristics of Von Kármán crater, northwestern South Pole-Aitken basin: Chang'E-4 landing site region. J. Geophys. Res. Planets 123, 1684–1700.
Hurwitz, D., Kring, D.A., 2015. Potential sample sites for South Pole–Aitken basin impact melt within the Schrödinger basin. Earth Planet. Sci. Lett. 427, 31–36.
Jia, Y., Zou, Y., Ping, J., Xue, C., Yan, J., Ning, Y., 2018. The scientific objectives and payloads of Chang'E−4 mission. Planet. Space Sci. 162, 207–215.
Jolliff, B.L., Shearer, C.K., Papanastassiou, D.A., Alkalai, L., MoonRise, T., 2010. MoonRise: South Pole-Aitken basin sample return mission for solar system science. In: 2010 Annual Meeting of the Lunar Exploration Analysis Group. Lunar and Planetary Institute, Washington, DC (abstract #3072).
Kalynn, J., Johnson, C.L., Osinski, G.R., Barnouin, O., 2013. Topographic characterization of lunar complex craters. Geophys. Res. Lett. 40, 38–42.
Klima, R.L., et al., 2011. New insights into lunar petrology: distribution and composition of prominent low-Ca pyroxene exposures as observed by the Moon Mineralogy Mapper (M^3). J. Geophys. Res. Planets 116, E00G06.
Lemelin, M., Lucey, P.G., Song, E., Taylor, G.J., 2015. Lunar central peak mineralogy and iron content using the Kaguya Multiband Imager: reassessment of the compositional structure of the lunar crust. J. Geophys. Res. Planets 120, 869–887.
Lemelin, M., Lucey, P.G., Miljković, K., Gaddis, L.R., Hare, T., Ohtake, M., 2019. The compositions of the lunar crust and upper mantle: spectral analysis of the inner rings of lunar impact basins. Planet. Space Sci. 165, 230–243.
Ling, Z., et al., 2015. Correlated compositional and mineralogical investigations at the Chang'e-3 landing site. Nat. Commun. 6, 8880.
Ling, Z., Jolliff, B.L., Liu, C., Qiao, L., Cao, H., Zhang, J., Fu, X., Li, B., Liu, J., 2019. A close view of Chang'e-4 landing site and science questions to be answered by Yutu-2. In: 50th Lunar and Planetary Science Conference. Lunar and Planetary Institute, The Woodlands, Texas (abstract #2330).
Lucey, P.G., 2004. Mineral maps of the Moon. Geophys. Res. Lett. 31, L08701.
Lucey, P., et al., 2006. Understanding the lunar surface and space-Moon interactions. Rev. Mineral. Geochem. 60, 83–219.
Melosh, H.J., 1989. Impact Cratering: A Geologic Process. Oxford University Press, London.
Melosh, H.J., 2011. Planetary Surface Processes. Cambridge University Press, Cambridge.
Melosh, H.J., et al., 2017. South Pole-Aitken basin ejecta reveal the Moon's upper mantle. Geology 45, 1063–1066.
Mimoun, D., et al., 2012. Farside explorer: unique science from a mission to the farside of the moon. Exp. Astron. 33, 529–585.
Morgan, J.V., et al., 2016. The formation of peak rings in large impact craters. Science 354, 878–882.
Moriarty III, D.P., Pieters, C.M., 2018. The character of South Pole-Aitken Basin: patterns of surface and subsurface composition. J. Geophys. Res. Planets 123, 729–747.
Morota, T., et al., 2011. Timing and characteristics of the latest mare eruption on the Moon. Earth Planet. Sci. Lett. 302, 255–266.
National Research Council, 2007. The Scientific Context for Exploration of the Moon. National Academy Press, Washington, D.C.
National Research Council, 2011. Vision and Voyages for Planetary Science in the Decade 2013–2022. National Academy Press, Washington, D.C.
Ohtake, M., et al., 2014. Geologic structure generated by large-impact basin formation observed at the South Pole-Aitken basin on the Moon. Geophys. Res. Lett. 41, 2738–2745.
Otake, H., Ohtake, M., Hirata, N., 2012. Lunar iron and titanium abundance algorithms based on SELENE (Kaguya) Multiband Imager data. In: 43rd Lunar and Planetary Science Conference. Lunar and Planetary Institute, The Woodlands, Texas (abstract #1905).
Papike, J.J., Hodges, F.N., Bence, A.E., Cameron, M., Rhodes, J.M., 1976. Mare basalts: crystal chemistry, mineralogy, and petrology. Rev. Geophys. 14, 475–540.
Pasckert, J.H., Hiesinger, H., van der Bogert, C.H., 2018. Lunar farside volcanism in and around the South Pole–Aitken basin. Icarus 299, 538–562.
Petro, N.E., Pieters, C.M., 2004. Surviving the heavy bombardment: ancient material at the surface of South Pole-Aitken Basin. J. Geophys. Res. Planets 109, E06004.
Pieters, C.M., Head, J.W., Gaddis, L., Jolliff, B., Duke, M., 2001. Rock types of South Pole-Aitken basin and extent of basaltic volcanism. J. Geophys. Res. Planets 106, 28001–28022.
Potter, R.W.K., Collins, G.S., Kiefer, W.S., McGovern, P.J., Kring, D.A., 2012. Constraining the size of the South Pole-Aitken basin impact. Icarus 220, 730–743.
Qiao, L., Head, J.W., Wilson, L., Kreslavsky, M.A., Xiao, L., 2016a. Compound flow fields in southwest Mare Imbrium: Geomorphology, source regions, and implications for lunar basin filling. In: 47th Lunar and Planetary Science Conference. Lunar and Planetary Institute, The Woodlands, Texas (abstract #2038).
Qiao, L., Liu, X., Zhao, J., Wei, Y., Xiao, L., 2016b. Geological investigations of Luna 17, Apollo 15 and Chang'E-3 landing sites at Mare Imbrium of the Moon (in Chinese). SCI. SIN. Phys. Mech. Astronom. 46, 029603.
Qiao, L., Xiao, Z., Zhao, J., Xiao, L., 2016c. Subsurface structures at the Chang'e-3 landing site: interpretations from orbital and in-situ imagery data. J. Earth Sci. 27, 707–715.
Robinson, M.S., et al., 2010. Lunar Reconnaissance Orbiter Camera (LROC) instrument overview. Space Sci. Rev. 150, 81–124.
Schultz, P.H., Crawford, D.A., 2011. Origin of nearside structural and geochemical anomalies on the Moon. Geol. Soc. Am. Spec. Pap. 477, 141–159.
Schultz, P.H., Crawford, D.A., 2016. Origin and implications of non-radial Imbrium Sculpture on the Moon. Nature 535, 391–394.
Smith, D.E., et al., 2010. The Lunar Orbiter Laser Altimeter investigation on the Lunar Reconnaissance Orbiter mission. Space Sci. Rev. 150, 209–241.
Spudis, P.D., 1993. The Geology of Multi-Ring Impact Basins. Cambridge University Press, Cambridge.
Sruthi, U., Kumar, P.S., 2014. Volcanism on farside of the Moon: new evidence from Antoniadi in South Pole Aitken basin. Icarus 242, 249–268.
Stuart-Alexander, D.E., 1978. Geologic Map of the Central Far Side of the Moon. United States Geological Survey Map 1–1047, Reston, VA.
Taylor, L.A., Pieters, C.M., Keller, L.P., Morris, R.V., McKay, D.S., 2001. Lunar mare soils: space weathering and the major effects of surface-correlated nanophase Fe. J. Geophys. Res. Planets 106, 27985–27999.
Tompkins, S., Pieters, C.M., 1999. Mineralogy of the lunar crust: results from Clementine. Meteorit. Planet. Sci. 34, 25–41.
Vaughan, W.M., Head, J.W., 2014. Impact melt differentiation in the South Pole-Aitken basin: some observations and speculations. Planet. Space Sci. 91, 101–106.
Wilhelms, D.E., 1993. To a Rocky Moon: A geologist's History of Lunar Exploration. University of Arizona Press, Tucson.
Wu, W.R., et al., 2017. Design of Chang'E-4 lunar farside soft-landing mission (in Chinese). J. Deep Space Explor. 4 (2), 111–117.
Yamamoto, S., et al., 2010. Possible mantle origin of olivine around lunar impact basins detected by SELENE. Nat. Geosci. 3, 533–536.
Yamamoto, S., et al., 2012. Olivine-rich exposures in the South Pole-Aitken Basin. Icarus 218, 331–344.
Yingst, R.A., Chuang, F.C., Berman, D.C., Mest, S.C., 2016. Geologic mapping of the Planck Quadrangle of the Moon (LQ-29). In: 47th Lunar and Planetary Science Conference. Lunar and Planetary Institute, The Woodlands, Texas (abstract #1188).
Zhang, J., et al., 2015. Volcanic history of the Imbrium basin: a close-up view from the lunar rover Yutu. Proc. Natl. Acad. Sci. 112, 5342–5347.